Harmonic modulation for ultrawide tuning range terahertz free-electron laser via frequency-beating laser modulation

Lingjun Tu,[1] Yifan Liang,[1] Hao Sun,[1] Li Zeng,[1] Huaiqian Yi,[1] Xinran Wang,[1] Yong Yu,[1] Jitao Sun,[1] Zhenbiao Sun,[1] Guorong Wu,[1] Baichao Zhang,[1] Hongfei Wang,[1] Jiahang Shao,[1] Xiaofan Wang,[1,*] Chao Feng,[2] Kaiqing Zhang,[2] Yin Kang,[2] Zhigang He,[3] Jiayue Yang,[3] Weiqing Zhang,[3,†] and Xueming Yang[3]

[1]*Institute of Advanced Light Source Facilities, Shenzhen 518107, China*
[2]*Shanghai Advanced Research Institute, Chinese Academy of Sciences, Shanghai 201210, China*
[3]*State Key Laboratory of Chemical Reaction Dynamics, Dalian Institute of Chemical Physics, Chinese Academy of Sciences, Dalian 116023, China*

(Received 26 February 2026; accepted 2 November 2026; published 16 November 2026)

Broadband tunability is a key pursuit for terahertz (THz) free-electron lasers, yet it is often constrained by the narrow energy acceptance of laser modulators in prebunched schemes. Here, we propose a harmonic modulation scheme to decouple this constraint. Taking the Electron Source Test Facility at Dalian as a specific case study, our simulations demonstrate that by matching the laser field to higher-order harmonic resonances of the undulator, we can obtain efficient energy modulation across a significantly wider electron energy range (40–130 MeV), surpassing the limit of 71–130 MeV imposed by the fundamental resonance. This technique facilitates continuous frequency tuning from 0.5 to 30 THz using a single modulator-radiator chain, establishing a versatile method for ultrabroadband THz generation.

DOI: 10.1103/w4s8-cchh

I. INTRODUCTION

Terahertz (THz) radiation has emerged as an important tool across diverse scientific frontiers. On the one hand, THz radiation provides direct access to collective low-energy degrees of freedom in condensed matter systems [1], such as lattice vibrations (phonons) [2,3], collective spin excitations (magnons) [4,5], and coherent quasiparticle interactions in correlated electron systems [6,7]. Intense THz fields allow nonperturbative manipulation of material states, including coherent interband polarization [8], field-driven phase transitions [9], large-amplitude spin oscillations [10], and the manipulation of quantum materials [11,12] as well as biomolecules [13]. At the same time, THz radiation serves as a powerful observational tool. Techniques such as terahertz scanning tunneling microscopy [14,15], terahertz spectroscopy [16,17], and terahertz scattering-type scanning near-field optical microscopy [18–20] rely on repeated measurements and therefore benefit from broad frequency tunability.

Relativistic electron beams can generate THz radiation via various emission pathways, including coherent synchrotron/edge radiation in bending magnets [21–23] and coherent transition/diffraction radiation at material interfaces or apertures [24–28]. Alternatively, by interacting with periodic magnetic structures, relativistic electron beams can drive free-electron lasers (FELs) to produce narrowband and continuously tunable THz radiation. Within the contemporary FEL landscape, FEL oscillators [28] provide high repetition rates up to 13 MHz with pulse energies up to approximately 2 μJ. Using nC-class high-brightness electron bunches, single-pass high-gain self-amplified spontaneous emission FEL pushes the THz pulse energy to the 100 μJ level [29]. To mitigate the slippage and diffraction effects, waveguide-assisted and strongly tapered zero-slippage configurations achieve approximately 10% average energy-extraction efficiency [30], but the frequency tuning range is limited [31]. A complementary route is provided by prebunched schemes, where microbunching is imposed at the radiator entrance to provide a coherent seed that is rapidly amplified to saturation [32,33]. In practice, appreciable THz-scale microbunching with broad frequency tunability can be generated either via nonlinear longitudinal space-charge dynamics [34,35] or via frequency-beating modulation [36–42]. Notably, these prebunched schemes achieve pulse energies up to hundreds of μJ with frequency coverage from approximately 1 THz up to few tens of THz.

*Contact author: wangxf@mail.iasf.ac.cn
†Contact author: weiqingzhang@dicp.ac.cn

Published by the American Physical Society under the terms of the Creative Commons Attribution 4.0 International license. Further distribution of this work must maintain attribution to the author(s) and the published article's title, journal citation, and DOI.

The Electron Source Test Facility (ESTF) serves as the high-brightness injector testbed for the proposed Dalian Advanced Light Source, a MHz-repetition-rate ultraviolet facility [43]. Currently, ESTF has been successfully commissioned, whereas the subsequent energy boosting stages (the main superconducting radiofrequency linac) for extreme ultraviolet operation are pending further construction phases. In this context, transforming the ESTF into a standalone user facility becomes a strategic priority, and various FEL schemes are under consideration to exploit its high-repetition-rate capabilities. Among them, the laser-beating prebunched scheme is particularly attractive for delivering fully coherent radiation. In this work, we focus on the performance evaluation and optimization of this specific scheme based on the current ESTF parameters. We demonstrate that while this approach is promising, its direct implementation faces bandwidth limitations, which we address through a harmonic modulation technique.

ESTF delivers high-quality electron beams with a nominal energy of 100 MeV. In a planar undulator, the radiation frequency f_r follows the resonant condition $f_r = 2c\gamma^2/\lambda_u(1 + K_u^2/2)$, where c is the speed of light in free space, γ is the beam relativistic factor, λ_u is the undulator period length, K_u is the undulator parameter. With a radiator period of $\lambda_u = 8$ cm, continuously tuning the undulator parameter K_u (4.75–14.8) at the nominal 100 MeV energy covers only the 3–20 THz range. To achieve the full 0.5–30 THz target, the electron beam energy must be tunable over a broad interval of 40–130 MeV. However, extending the operation of the prebunched scheme to this wide energy range reveals a critical mismatch in the seed laser modulator. Given a modulator period λ_m of 3 cm and a seed laser wavelength λ_s of 800 nm, the achievable undulator parameter K_m range (0.28–2.41) restricts the fundamental resonance to electron energies between 71 and 130 MeV. Consequently, the low-energy window (40–71 MeV), which is essential for generating the 0.5–1.7 THz FEL, becomes inaccessible to the modulation process.

To overcome this fundamental limitation and fully exploit the target 40–130 MeV energy range, we introduce the systematic use of harmonic modulation [44–46]. By setting the modulator resonant at integer multiples of the seed laser wavelength, energy modulation is efficiently achieved even for lower-energy electron beams. Specifically, for the 40–60 MeV range, the modulator is tuned to a fundamental wavelength of 4000 nm to interact with the 800 nm seed laser at the fifth harmonic ($n = 5$); for 60–75 MeV, it is tuned to 2400 nm (third harmonic, $n = 3$); and for 75–130 MeV, it operates at the 800 nm fundamental ($n = 1$). This technique successfully extends the resonantly modulated electron energy range from 71–130 MeV down to 40 MeV, thereby broadening the achievable THz FEL radiation range to 0.5–30 THz. While this facility-dictated tuning range does not yet fully encompass the lower sub-THz (< 0.5 THz) and higher mid-infrared (> 30 THz) frequencies, the proposed integration strategy imposes no fundamental restriction on access to these broader spectra.

II. PHYSICAL IMPLEMENTATION AND PRINCIPLE

The implementation of the proposed harmonic modulation scheme at the ESTF is illustrated in Fig. 1. As shown in the top panel, the beamline comprises a superconducting linac, a laser modulator, a magnetic bunch compressor, and

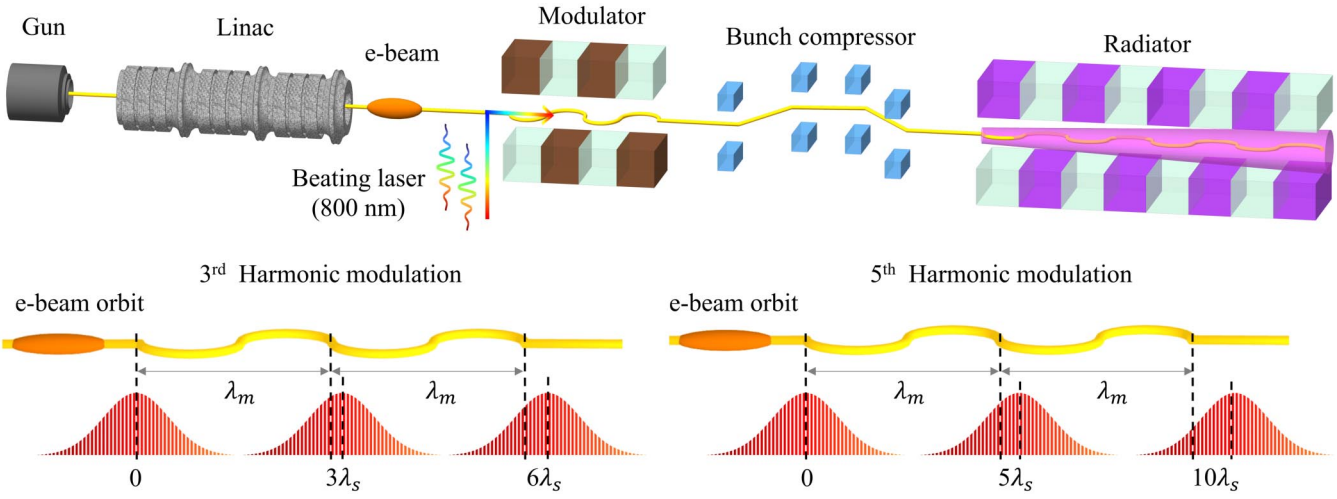


FIG. 1. Principle of harmonic modulation in a prebunched THz FEL from frequency-beating modulation. Top: Conceptual beamline layout. Bottom: Illustration of the nth harmonic modulation. Under resonance at $n\lambda_s$, the laser slips ahead of the electrons by $n\lambda_s$ per modulator period λ_m. Shown are the $3\lambda_s$ (left) and $5\lambda_s$ (right) slippages for the third- and fifth-harmonic modulation.

TABLE I. Typical parameters at ESTF.

Parameter	Value
Electron beam	
Electron energy E	40–130 MeV
Bunch charge	500 pC
Initial current I	80 A
Bunch length	6.25 ps
Emittance ϵ	1.0 mm mrad
Slice energy spread σ_E	0.01%
Modulator	
Period λ_m	3 cm
Period number	10
Undulator parameter K_m	0.28–2.41
Radiator	
Period λ_u	8 cm
Period number	50
Undulator parameter K_u	4.75–14.8

a THz radiator. In this configuration, the modulator is resonant at the seed laser wavelength λ_s, while the radiator is tuned to the beat frequency. The main electron beam and undulator parameters are summarized in Table I. Here, we assume an ideal electron beam with a charge of 500 pC, a flat current of 80 A, a normalized emittance of 1.0 mm mrad, and an rms relative energy spread of 0.01%. In this setup, the electron beam is generated by a photocathode gun and accelerated to a nominal energy of 100 MeV in the superconducting linac before entering a 10-period laser modulator ($\lambda_m = 30$ mm). Energy modulation is imposed by the seed laser following the harmonic resonant condition depicted in the bottom panel of Fig. 1.

The energy modulation process in the modulator satisfies the resonance condition [46]:

$$\gamma^2 = \frac{\lambda_m}{2n\lambda_s}\left(1 + \frac{K_m^2}{2}\right), \tag{1}$$

where n denotes the harmonic number of the laser-electron interaction. In practice, the accessible resonance range of electron energy in Eq. (1) is constrained by the achievable undulator parameter K_m of the laser modulator. At ESTF, the modulator plans to employ a NdFeB permanent-magnet undulator with a period of $\lambda_m = 3$ cm, for which the undulator parameter K_m is determined by the magnet gap according to the Halbach formula [47]. The peak magnetic field for a NdFeB undulator is estimated as

$$B_0[\mathrm{T}] \approx 3.44 \exp\left[-\frac{g}{\lambda_m}\left(5.08 - 1.54\frac{g}{\lambda_m}\right)\right], \tag{2}$$

leading to $K_m \approx 0.934\ B_0[\mathrm{T}]\lambda_m[\mathrm{cm}]$. Assuming a practical magnet gap range of $g = 9$–30 mm, the corresponding K_m varies from 0.28 to 2.41.

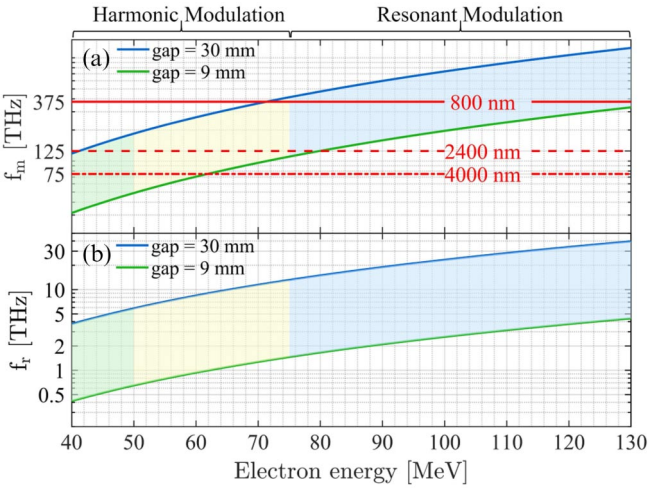


FIG. 2. Resonance coverage of the modulator [panel (a)] and the THz radiator [panel (b)] as a function of electron energy. In panel (a), the shaded regions indicate the operating regimes of fifth-harmonic (light green), third-harmonic (light yellow), and resonant (light blue) modulation. Panel (b) shows the corresponding THz radiation coverage, illustrating the extension of the tunable range down to 0.5 THz enabled by harmonic modulation at low electron energies.

To quantitatively illustrate how harmonic modulation extends the accessible energy-modulation range under realistic engineering constraints, Fig. 2 compares the resonance coverage of the laser modulator with that of the THz radiator. As shown in Fig. 2(a), the resonance coverage of the modulator is plotted as a function of electron energy. Here, $f_m = 2c\gamma^2/\lambda_m(1 + K_m^2/2)$ is the resonant frequency of the modulator. The blue and green solid curves correspond to the resonance boundaries defined by the maximum and minimum undulator gaps of 30 and 9 mm, respectively, with the shaded area between them representing the achievable tuning range of the modulator. The fixed seed-laser wavelength of 800 nm is indicated by the red solid line. Within the available gap range, fundamental resonance with the seed laser is only satisfied for electron energies above approximately 71 MeV (75 MeV with a conservative margin), leaving the lower-energy region inaccessible under conventional resonant modulation. By operating the modulator at higher-order harmonic resonances of the same seed laser, the fundamental resonance condition is shifted to longer wavelengths, as indicated by the red dashed and dot-dashed lines corresponding to the third- and fifth-harmonic configurations. Their intersections with the tunable region defined by the undulator gap demonstrate that efficient energy modulation remains feasible for electron energies down to 40 MeV within the same hardware configuration.

Figure 2(b) shows the corresponding frequency coverage of the THz radiator for electron energies from 40 to 130 MeV, taking into account the same undulator gap

range of 9–30 mm. The radiation frequency of the THz radiator follows the fundamental resonance condition, determined by the electron energy and the undulator parameters. Equivalently, the resonant radiation wavelength is $\lambda_r = c/f_r$. When only resonant modulation is available at electron energies above 75 MeV, the lower bound of the radiation frequency is limited to approximately 1.7 THz. With the extended energy-modulation window enabled by harmonic modulation, the full electron-energy range required by the radiator is accessed, allowing continuous THz frequency coverage down to 0.5 THz.

III. RESULTS

In this section, we present start-to-end numerical results demonstrating the performance of the proposed scheme for ultrabroadband THz FEL generation. The achievable tuning range, modulation efficiency, and FEL output characteristics across the entire 0.5–30 THz band are quantitatively evaluated under realistic accelerator and laser constraints. The frequency-beating process is numerically simulated based on the superposition of chirped Gaussian pulses. The modulation of the electron beam is simulated using ELEGANT [48] with second-order transport effects taken into account. The THz FEL lasing processes were simulated using the time-dependent mode of GENESIS [49]. Nonlinear effects such as coherent synchrotron radiation (CSR), incoherent synchrotron radiation, and longitudinal space charge effects are also included in these simulations.

A. Generation of frequency-beating laser

The performance of the frequency-beating laser is first evaluated, as it directly determines the accessible beat frequency and the effective longitudinal overlap with the electron bunch in the proposed scheme. As illustrated in Fig. 3, an ultrafast Ti:sapphire laser pulse is temporally stretched by a grating-pair stretcher and subsequently split into two replicas. After introducing a controllable time delay τ between the two stretched pulses, they are recombined to generate a beating optical field with a well-defined THz-scale intensity.

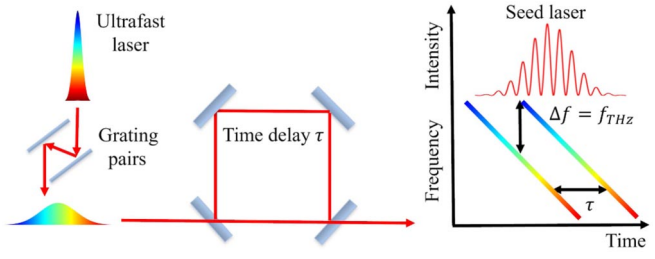


FIG. 3. Schematic layout of the frequency-beating laser. The pulse is stretched by grating pairs and split into two branches. A tunable time delay τ between the recombined chirped pulses generates a beat note at the THz frequency f_{THz}, which is linearly controllable by τ.

For a Gaussian pulse, the grating stretcher increases its width to [36]:

$$\sigma_{\mathrm{out}} = \sigma_0 \left(1 + 4\frac{\varphi_2^2}{\sigma_0^4}\right)^{\frac{1}{2}}. \tag{3}$$

Here, σ_0 and σ_{out} are the input and stretched electric-field $1/e$ half-widths, respectively. The group delay dispersion is [36]:

$$\varphi_2 = -\frac{4\pi^2 cL}{\omega_0^3 d^2}\left[1 - \left(\frac{2\pi c}{\omega_0 d} - \sin\theta\right)^2\right]^{-\frac{3}{2}}. \tag{4}$$

Here, L is the separation between the grating pair, d is the groove spacing, θ is the incident angle, and ω_0 is the central angular frequency of the laser. The relative time delay τ between the two stretched pulses sets the beat frequency, which under the linear-chirp approximation is written as

$$f = \frac{\tau}{\pi\sigma_0\sigma_{\mathrm{out}}}, \tag{5}$$

enabling continuous tuning of the beat frequency. In practice, $\tau \gg 10$ fs is required to ensure a robust and well-defined beating, given that timing jitter induced by laser pointing and other effects are on the order of ~10 fs.

The simulations use parameters representative of an 800-nm Ti:sapphire laser [50], as summarized in Table II. The Gaussian input pulse has $\sigma_0 = 15$ fs, a waist radius of 1.5 mm, and a peak power of 50 GW, corresponding to an energy of 0.94 mJ. The grating pair stretches the pulse to $\sigma_{\mathrm{out}} = 3.92$ ps, with a peak power of 47.8 MW per replica. By varying the time delay τ from 92 fs to 5.53 ps, a continuously tunable frequency-beating signal spanning 0.5–30 THz is obtained. The peak power of the beating

TABLE II. Parameters of the frequency-beating laser system.

Parameter	Value
Ultrafast laser	
Wavelength λ_s	800 nm
Peak power P_L	50 GW
Input pulse width σ_0	15 fs
Pulse energy	0.94 mJ
Waist radius	1.5 mm
Frequency-beating process	
Grating pairs distance L	30 mm
Groove density $1/d$	1000 lines/mm
Incident angle θ	35°
Stretched pulse width σ_{out}	3.92 ps
Peak power per stretched replica	47.8 MW
Time delay τ	0.092–5.53 ps

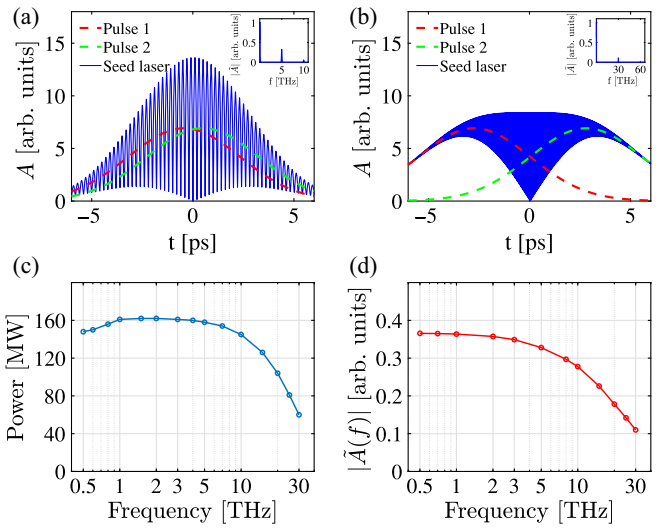


FIG. 4. Performance of the frequency-beating laser. Electric-field amplitude profile of the frequency-beating laser at 5 THz [panel (a)] and 30 THz [panel (b)]; insets display the corresponding Fourier spectra. Peak power [panel (c)] and normalized spectral amplitude [panel (d)] evaluated at the imposed beat frequency.

pulse is evaluated by rescaling the peak power of the stretched pulse according to the squared ratio of their peak field amplitudes, assuming an overall optical efficiency of 0.85.

Figures 4(a) and 4(b) show representative temporal electric-field amplitude profiles of the frequency-beating laser at 5 and 30 THz, respectively. The red and green dashed curves represent the electric-field amplitudes of the two stretched pulses after passing through the beam splitter, while the blue solid curve denotes the resulting longitudinal amplitude distribution after recombination. In both cases, a quasisinusoidal amplitude is formed within the stretched-pulse envelope. The corresponding Fourier spectra, shown in the insets, exhibit distinct peaks at the imposed beat frequencies, confirming precise frequency control and stable spectral purity across the entire THz tuning range. A comparison between Figs. 4(a) and 4(b) shows that increasing the delay τ not only sets the beat frequency according to Eq. (5), but also progressively separates the centers of the two stretched pulses, thereby introducing an intrinsic trade-off between frequency tunability and pulse overlap. As τ becomes larger, the overlap between the pulses decreases, modifying both the peak amplitude and the overall envelope of the beating signal. Consequently, the peak power of the recombined beating pulse varies with τ.

The dependence of the beating-pulse peak power on the beat frequency, from 0.5 to 30 THz, is plotted in Fig. 4(c). For frequencies between 0.5 and 2 THz, where $\tau \ll \sigma_{\text{out}}$, the two stretched pulses remain nearly overlapped; thus, the peak power fluctuates slightly between 150 and 162 MW due to phase-interference effects. In the 2–30 THz range, the centers of the two Gaussian pulses gradually separate, causing the peak power of the beating signal to decrease from approximately 162 to 60 MW. Figure 4(d) plots the normalized spectral amplitude at the beat frequency extracted from the Fourier spectra. As the delay τ increases, the interaction between the two stretched pulses weakens, leading to a monotonic decrease of the normalized spectral amplitude from 0.37 to 0.10. At 30 THz, the required delay $\tau = 5.53$ ps is comparable to σ_{out}, approaching the practical tuning limit. Further increasing τ would lead to a dramatic reduction in the normalized spectral amplitude.

The frequency-beating pulse provides a tunable temporal structure for longitudinal energy modulation of the 6.25-ps electron bunch. The attainable peak-power range and precise controllability of the beat frequency across the 0.5–30 THz beat frequencies establish the operational parameter space of the laser system. The effectiveness of the resulting energy modulation will be quantitatively examined in the next subsection.

B. Laser-beam modulation and microbunching

The frequency-beating laser interacts with the electron beam in the 30-mm-period, 10-period modulator, imprinting an optical-wavelength (800 nm) sinusoidal energy modulation whose envelope is governed by the longitudinal amplitude profile of the frequency-beating laser. Assuming a Gaussian transverse profile for the seed laser with an rms size σ_r, the energy modulation for electrons at the laser transverse center is given by [44]

$$\Delta\gamma = \sqrt{\frac{P_L}{P_0}}\frac{K_m L_m}{\gamma\sigma_r} JJ_n, \tag{6}$$

where P_L is the peak laser power, $P_0 \approx 8.7$ GW, and L_m is the undulator length. The coupling factor JJ_n characterizes the coupling efficiency of the laser-electron interaction at the nth harmonic

$$JJ_n = J_{(n-1)/2}\left(\frac{nK_m^2}{4+2K_m^2}\right) - J_{(n+1)/2}\left(\frac{nK_m^2}{4+2K_m^2}\right), \tag{7}$$

with J_i denoting the Bessel function of the ith order.

After the energy modulation, the electron beam passes through a magnetic chicane with the dispersion strength R_{56}. Neglecting collective effects, the longitudinal time coordinate of an electron becomes

$$t_1 = t + \frac{R_{56}\Delta\gamma}{c\gamma}. \tag{8}$$

The effectiveness of this energy-to-density conversion is quantified by the bunching factor, $b = \langle e^{i\psi}\rangle$, where ψ

denotes the ponderomotive phase of the electrons with respect to the imposed modulation. Accordingly, for each target THz frequency, R_{56} is scanned to obtain sufficient microbunching. In practice, the choice of R_{56} is also constrained by CSR, since a larger R_{56} requires stronger bending in the designed chicane. The stronger bending enhances CSR-induced energy variations, which are converted by the lattice dispersion into increased energy spread and projected horizontal emittance. Therefore, R_{56} is selected by balancing sufficient microbunching against acceptable CSR-induced beam degradation.

In the designed beamline, a 5-m chicane provides a maximum momentum compaction of $R_{56} \approx 200$ mm, which is sufficient to generate measurable microbunching at 0.5 THz and exceeds the requirement for frequencies above 1 THz. For the maximum R_{56} of 200 mm, the energy loss from CSR is analytically estimated to be several tens of keV, and the projected horizontal emittance grows to 1.65 mm mrad, while these impacts diminish for smaller R_{56}.

Figure 5 shows the longitudinal phase space and current profiles at the entrance of the THz radiator. Figures 5(a) and 5(b) correspond to 0.5 and 1 THz, generated via fifth-harmonic modulation at 40 MeV and third-harmonic modulation at 60 MeV, respectively. Clear microbunching is observed in these cases, with current spikes appearing at periods of 2 and 1 ps, corresponding exactly to microbunching frequencies of 0.5 and 1 THz. In the fifth-harmonic case shown in Fig. 5(a), $R_{56} = 200$ mm yields a peak current of about 95 A and a maximum bunching factor of $b \approx 0.07$. For the third-harmonic case in Fig. 5(b), $R_{56} = 130$ mm produces a peak current of 170 A with $b \approx 0.32$. Although the phase spaces show signs of CSR-induced energy loss, the microbunching structure remains distinct.

Figures 5(c)–5(e) present a representative high-frequency example at 10 THz, which is generated via fundamental modulation at 100 MeV. In Fig. 5(c), the optimized $R_{56} = 12$ mm yields a peak current of 150 A and a maximum bunching factor of $b \approx 0.31$. The Fourier transform of the current profile in Fig. 5(e) exhibits a clear peak at 10 THz, verifying strong microbunching at the imposed frequency. To resolve the fine-scale structure, Fig. 5(d) displays a close-up region from 3 to 3.3 ps, where three 10-THz cycles are clearly visible with a peak-to-peak spacing of 0.1 ps. Within each cycle, ~37 alternating bright-dark stripes originating from the 800-nm seed laser are observed on top of the THz-period modulation. In addition, the simulated energy modulation amplitudes align with analytical estimates [Eqs. (6) and (7)] of approximately 36, 110, and 170 keV, respectively.

The achievable bunching factor across the entire tuning range is summarized in Fig. 5(f). In the frequency range below 1 THz, the bunching factor is limited to ~0.10. This is primarily attributed to the reduced energy modulation amplitude resulting from the weaker coupling efficiency

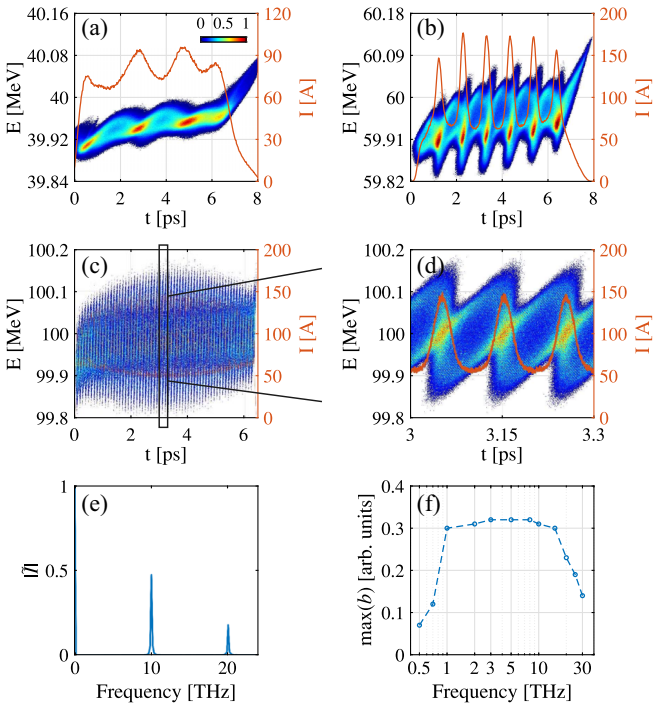


FIG. 5. Characteristics of the prebunched electron beam. Longitudinal phase spaces and current profiles are shown for: the 0.5 THz case using fifth-harmonic modulation at 40 MeV [panel (a)] and the 1 THz case using third-harmonic modulation at 60 MeV [panel (b)]. Panels (c)–(e) display a representative high-frequency case at 10 THz, including the full phase space [panel (c)], a close-up phase-space region highlighting the subcycle structure [panel (d)] and the longitudinal current spectrum [panel (e)]. Panel (f) summarizes the maximum bunching factor as a function of the target frequency.

(JJ_n) of the fifth-harmonic interaction. Constrained by the maximum available dispersion strength (R_{56}), this limited energy modulation is insufficient to fully maximize the bunching factor. While this value is lower than that of the fundamental case, it remains acceptable for extending the modulation window toward lower electron energies in the present parameter regime. In contrast, the bunching factor remains robust (~0.3) between 1 and 15 THz, before gradually dropping to 0.14 at 30 THz due to the reduced peak power and spectral amplitude of the beating laser [Figs. 4(c)–4(d)].

Overall, these results demonstrate that harmonic-assisted modulation effectively generates sufficient microbunching across the 0.5–30 THz range to drive coherent emission and initiate strong FEL interaction. In the following section, we analyze the evolution of these prebunched beams in the THz radiator and characterize the resulting FEL gain and output.

C. Generation of THz radiation

Owing to the finite bunching factor at the radiator entrance, the interaction starts from a coherently emitted

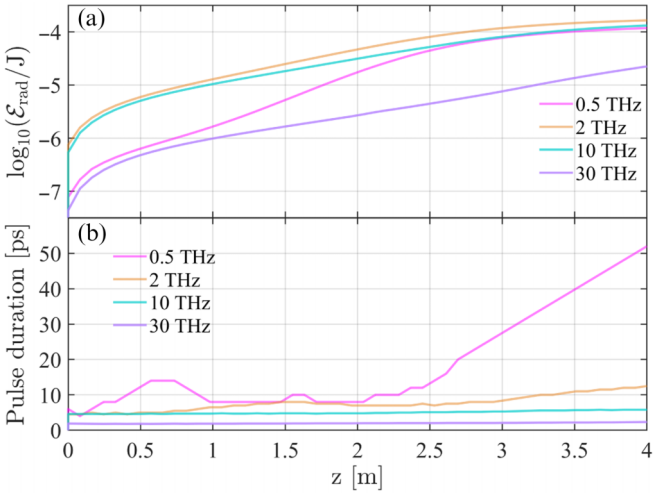


FIG. 6. Evolution of the THz FEL radiation along the 4-m radiator for representative frequencies (0.5, 2, 10, and 30 THz). Pulse-energy growth showing the different gain lengths and saturation behaviors [panel (a)]. Evolution of the radiation pulse duration (FWHM), illustrating the increasing influence of slippage at low frequencies and the reduced gain at high frequencies [panel (b)].

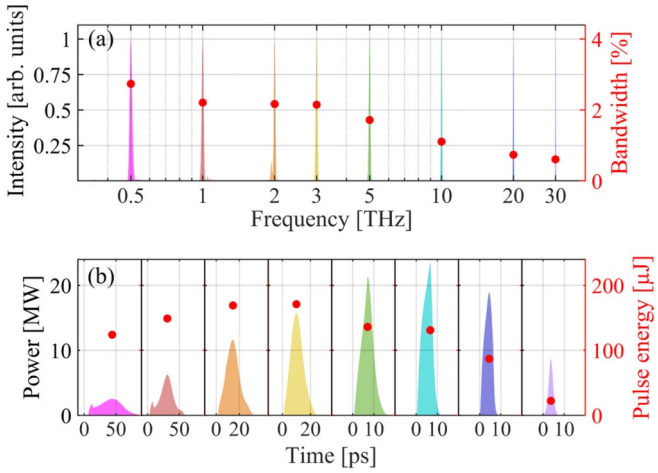


FIG. 7. Performance of THz radiation of different frequency in the range of 0.5–30 THz at the exit of the 4-m undulator. Panel (a) displays the output spectra as shaded curves on the left axis and the relative bandwidths as red dots on the right axis. Panel (b) shows the temporal power profiles as shaded curves on the left axis and the total pulse energies as red dots on the right axis.

radiation field rather than from shot noise, placing the FEL operation in a prebunched regime. In this case, the initial radiation power is determined by the bunching-induced coherent emission, scaling as $P_{\rm coh} \propto b^2$ [32], while the subsequent growth and saturation are governed by the Pierce parameter ρ. For the one-dimensional case, ρ scales approximately $\rho \propto \sqrt[3]{(\gamma/f_r^2)}$ [51]. As a result, achieving a large saturated power becomes increasingly difficult at higher frequencies. Meanwhile, the slippage effect imposes additional limitations at lower frequencies. In an undulator, the radiation wavefront slips ahead of the electrons by $N\lambda_r$ after every N periods. For smaller frequency in the THz range, the slippage length within a few undulator periods is comparable to the bunch length.

To assess performance of the prebunched electron beams in the radiator across the tuning range, Fig. 6 shows the FEL gain evolution for four representative frequencies. Figure 6(a) presents the evolution of the pulse energy $\mathcal{E}_{\rm rad}$ at 0.5, 2, 10, and 30 THz along the undulator position z. In the first meter of the radiator, the pulse energy differs among frequencies due to the different initial bunching factors. During the exponential gain stage, the gain length increases monotonically with frequency, with values of 0.434, 0.790, 0.905, and 1.01 m for 0.5, 2, 10, and 30 THz, respectively. The FEL at 0.5, 2, and 10 THz reaches saturation at undulator lengths of about 2.5, 2.5, and 3.5 m, whereas the 30 THz radiation does not reach saturation within the 4-m radiator, consistent with its reduced Pierce parameter at high frequency.

Figure 6(b) shows the evolution of the FEL pulse duration (FWHM) at the same frequencies. The evolution of the radiation pulse duration further reflects the interplay between prebunching and slippage. For 0.5, 2, and 10 THz, the radiation initially exhibits a pulse width of approximately 5 ps, slightly shorter than the 6.25-ps electron bunch. In contrast, the 30-THz case begins with a much narrower radiation pulse of about 1.5 ps, since the bunching is concentrated near the bunch center where the beating-laser amplitude is largest. During the exponential gain stage, the radiation is generated locally along the electron beam, so the increase of the FEL pulse duration proceeds much more slowly than the nominal slippage rate. Near saturation, however, the slippage becomes prominent for the two low-frequency cases (0.5 and 2 THz), as evidenced by the noticeable broadening in their pulse-duration curves. For 10 and 30 THz, the total slippage length remains much smaller than the bunch duration, and its influence on gain is negligible. Collectively, Fig. 6 illustrates the evolution of FEL characteristics across the ultrawide tuning range, confirming the expected shift from slippage-dominated pulse elongation at low frequencies to slower gain growth at high frequencies.

Figure 7 summarizes the spectral and temporal characteristics of the THz FEL at the radiator exit across the full tuning range. The results illustrate how the combined effects of initial prebunching, FEL gain, and slippage shape the properties of the emitted THz pulses. Figure 7(a) presents the spectral intensity and the FWHM bandwidth for the eight representative frequencies. The relative bandwidth narrows from 2.74% at 0.5 THz to 0.61% at 30 THz. The corresponding temporal power profiles are displayed in Fig. 7(b). As the frequency increases, the peak power $P_{\rm peak}$ initially rises and then declines, reaching a

TABLE III. Summary of simulated THz FEL performance with frequencies in range of 0.5–30 THz at the 4-m radiator exit.

Frequency (THz)	Electron energy (MeV)	Modulation harmonic n	Relative bandwidth (%)	Pulse duration (ps)	Pulse energy (μJ)	Peak power (MW)	Waist radius (mm)	E_{eff} (MV/cm)
0.5	40	5	2.74	52	118	2.7	0.30	0.85
1.0	60	3	2.21	19	150	6.2	0.15	2.6
2.0	80	1	2.17	13	164	11	0.10	5.1
3.0	100	1	2.15	10	172	15	0.10	6.0
5.0	100	1	1.72	5.8	136	20	0.10	6.9
10.0	100	1	1.11	5.8	131	23	0.10	7.4
20.0	100	1	0.74	4.9	87	19	0.10	6.8
30.0	130	1	0.61	2.3	22	8.6	0.10	4.6

maximum of 23 MW at 10 THz. The variation in bandwidth is understood by analyzing the interplay between the pulse shape and the number of optical cycles, considering that the relative bandwidth inherently scales inversely with the cycle count. At 0.5 THz, the radiation pulse has a FWHM duration of approximately 52 ps, corresponding to about 26 optical cycles, and a relative spectral FWHM bandwidth of 2.74%. At 30 THz, although the pulse duration is as short as 2.3 ps, the pulse envelope contains ∼70 optical cycles, which is substantially larger than in the 0.5 THz case. This high number of optical cycles directly contributes to the observed spectral narrowing. Furthermore, as indicated in Fig. 5, the intensity of the initial microbunching gradually decreases toward the edges due to the Gaussian-like envelope of the beating laser. At 30 THz, the radiation pulse shape follows the Gaussian-like bunching profile. Consequently, the generated radiation originates from this Gaussian-like bunching profile with minimal slippage-induced distortion, yielding a clean temporal structure that corresponds to high monochromaticity with a bandwidth of only 0.61%.

Here, the reference cases are presented without additional optimization of pulse duration or spectral purity to provide a consistent comparison of the bunching and gain characteristics obtained with harmonic and fundamental modulation. Their temporal and spectral properties can nevertheless be tailored. In particular, continued interaction after saturation contributes to pulse lengthening at 0.5 THz and spectral splitting at 2 THz: slippage further broadens the radiation pulse, while electron-energy loss shifts the resonance toward lower frequencies. These effects can be mitigated by delaying saturation toward the undulator exit. This can be achieved through suitable undulator tapering or resonance detuning, or by lowering the modulation-laser intensity to reduce the initial bunching. Such adjustments involve performance trade-offs: pulse shortening can be accompanied by spectral broadening, whereas reduced initial bunching can lower the output pulse energy.

One possible configuration combines a reverse taper with a subsequent conventional taper [52,53]. The first section suppresses radiation growth while preserving strong bunching, whereas the second compensates for electron-energy loss and promotes energy extraction from the prebunched beam. Our simulations of two consecutive 2-m undulators, with the intervening drift omitted, show that a selected taper setting shortens the 0.5 THz pulse to around 20 ps and increases its energy, while broadening the relative spectral FWHM bandwidth to approximately 8%. However, during conventional FEL operation, THz diffraction across the break can reduce the radiation-electron beam overlap and weaken subsequent amplification. A practical two-undulator configuration would also require electron-radiation phase matching and beam-orbit control. These spectral and engineering trade-offs favor retaining the single 4-m radiator as the baseline configuration.

Detailed performance metrics for all representative frequencies are summarized in Table III, including specific values for bandwidth, pulse duration, pulse energy, and peak power. The results show that stable pulse energy at 100-μJ level is successfully achieved across 0.5–20 THz. Notably, at the lower frequency limit of 0.5 THz, the system maintains a high pulse energy of 118 μJ, confirming that the harmonic modulation is sufficient to drive the FEL to saturation even at low electron energies. In addition to these fundamental FEL properties, the table also lists the estimated focused waist size and the corresponding effective electric field (E_{eff}), as the facility is specifically targeted at high-field THz applications. The effective electric field is derived from the simulated peak power and the focused waist size using standard electromagnetic relations. The achievable waist radius w_0 is determined by the dominant limiting factor between the optical diffraction limit and the electron beam dimension, estimated as $w_0 \approx \max(\lambda/2, 0.1\ \mathrm{mm})$. Using an effective focal area πw_0^2 to estimate the electric field as $E_{\mathrm{eff}} \approx \sqrt{2P_{\mathrm{peak}}/(\pi w_0^2 c\epsilon_0)}$, where ϵ_0 is the vacuum permittivity, the resulting effective electric fields span from 0.85 to 7.4 MV/cm across the tuning range.

IV. CONCLUSION

In this work, we have proposed and systematically employed the harmonic modulation scheme to overcome

the intrinsic resonance limitation of laser-based prebunched THz free-electron lasers. By exploiting higher-order harmonic modulations in the laser modulator, the effective energy-modulation window is significantly extended without altering the seed-laser wavelength or the undulator hardware.

Applied to the ESTF THz FEL, this approach expands the resonantly accessible electron-energy range from 71–130 down to 40 MeV, enabling continuous and coherent THz radiation covering 0.5–30 THz within a single beamline. Start-to-end simulations demonstrate that stable microbunching and efficient FEL gain are achieved across the entire tuning range, yielding pulse energies around the 100 μJ level and narrow relative bandwidths of a few percent.

Beyond the specific implementation at ESTF, this work introduces harmonic modulation as a general and practical strategy to relax the resonance constraints of laser modulation. This concept provides a versatile and hardware-efficient pathway to extend both the accessible radiation frequency and the allowable electron-energy range in prebunched FEL schemes. As such, it can be applied to other FEL facilities where the mismatch between electron energy, seed-laser wavelength, and modulator parameters limits the operational lasing frequency or wavelength coverage.

ACKNOWLEDGMENTS

This work is supported by the Scientific Instrument Developing Project of Chinese Academy of Sciences (Grant No. GJJSTD20220001), the National Natural Science Foundation of China (Grants No. 12605510 and No. 22288201), DICP (Grant No. DICP I202304), the Strategic Priority Research Program of the Chinese Academy of Sciences: XDB0970000 (subject: XDB0970100) and LiaoNing Revitalization Talents Program XLYC2202030.

DATA AVAILABILITY

There are no publicly available research data or software supporting this manuscript. Requests for further information or data should be sent to the authors.

[1] P. A. Banks, E. M. Kleist, and M. T. Ruggiero, Investigating the function and design of molecular materials through terahertz vibrational spectroscopy, Nat. Rev. Chem. **7**, 480 (2023).

[2] S. Maehrlein, A. Paarmann, M. Wolf, and T. Kampfrath, Terahertz sum-frequency excitation of a Raman-active phonon, Phys. Rev. Lett. **119**, 127402 (2017).

[3] S. Fava, G. De Vecchi, G. Jotzu, M. Buzzi, T. Gebert, Y. Liu, B. Keimer, and A. Cavalleri, Magnetic field expulsion in optically driven $YBa_2Cu_3O_{6.48}$, Nature (London) **632**, 75 (2024).

[4] J. Lu, X. Li, H. Y. Hwang, B. K. Ofori-Okai, T. Kurihara, T. Suemoto, and K. A. Nelson, Coherent two-dimensional terahertz magnetic resonance spectroscopy of collective spin waves, Phys. Rev. Lett. **118**, 207204 (2017).

[5] Z. Wang, C.-M. Halati, J.-S. Bernier, A. Ponomaryov, D. I. Gorbunov, S. Niesen, O. Breunig, J. M. Klopf, S. Zvyagin, T. Lorenz *et al.*, Experimental observation of repulsively bound magnons, Nature (London) **631**, 760 (2024).

[6] T. Suzuki and R. Shimano, Time-resolved formation of excitons and electron-hole droplets in Si studied using terahertz spectroscopy, Phys. Rev. Lett. **103**, 057401 (2009).

[7] F. Langer, M. Hohenleutner, C. P. Schmid, C. Pöllmann, P. Nagler, T. Korn, C. Schüller, M. S. Sherwin, U. Huttner, J. T. Steiner *et al.*, Lightwave-driven quasiparticle collisions on a subcycle timescale, Nature (London) **533**, 225 (2016).

[8] O. Schubert, M. Hohenleutner, F. Langer, B. Urbanek, C. Lange, U. Huttner, D. Golde, T. Meier, M. Kira, S. W. Koch *et al.*, Sub-cycle control of terahertz high-harmonic generation by dynamical Bloch oscillations, Nat. Photon. **8**, 119 (2014).

[9] M. Liu, H. Y. Hwang, H. Tao, A. C. Strikwerda, K. Fan, G. R. Keiser, A. J. Sternbach, K. G. West, S. Kittiwatanakul, J. Lu *et al.*, Terahertz-field-induced insulator-to-metal transition in vanadium dioxide metamaterial, Nature (London) **487**, 345 (2012).

[10] E. A. Mashkovich, K. A. Grishunin, R. V. Mikhaylovskiy, A. K. Zvezdin, R. V. Pisarev, M. B. Strugatsky, P. C. M. Christianen, T. Rasing, and A. V. Kimel, Terahertz optomagnetism: Nonlinear THz excitation of GHz spin waves in antiferromagnetic $FeBO_3$, Phys. Rev. Lett. **123**, 157202 (2019).

[11] X. Yang, C. Vaswani, C. Sundahl, M. Mootz, P. Gagel, L. Luo, J. H. Kang, P. P. Orth, I. E. Perakis, C. B. Eom *et al.*, Terahertz-light quantum tuning of a metastable emergent phase hidden by superconductivity, Nat. Mater. **17**, 586 (2018).

[12] C.-J. Yang, J. Li, M. Fiebig, and S. Pal, Terahertz control of many-body dynamics in quantum materials, Nat. Rev. Mater. **8**, 518 (2023).

[13] D. A. Turton, H. M. Senn, T. Harwood, A. J. Lapthorn, E. M. Ellis, and K. Wynne, Terahertz underdamped vibrational motion governs protein-ligand binding in solution, Nat. Commun. **5**, 3999 (2014).

[14] T. L. Cocker, V. Jelic, M. Gupta, S. J. Molesky, J. A. J. Burgess, G. D. L. Reyes, L. V. Titova, Y. Y. Tsui, M. R. Freeman, and F. A. Hegmann, An ultrafast terahertz scanning tunnelling microscope, Nat. Photon. **7**, 620 (2013).

[15] K. Kimura, R. Tamaki, M. Lee, X. Ouyang, S. Kusaba, R. B. Jaculbia, Y. Kawada, J. Jung, A. Muranaka, H. Imada *et al.*, Ultrafast on-demand exciton formation in a single-molecule junction by tailored terahertz pulses, Science **387**, 1077 (2025).

[16] B. Ferguson and X.-C. Zhang, Materials for terahertz science and technology, Nat. Mater. **1**, 26 (2002).

[17] P. U. Jepsen, D. G. Cooke, and M. Koch, Terahertz spectroscopy and imaging–modern techniques and applications, Laser Photonics Rev. **5**, 124 (2011).
[18] A. J. Huber, F. Keilmann, J. Wittborn, J. Aizpurua, and R. Hillenbrand, Terahertz near-field nanoscopy of mobile carriers in single semiconductor nanodevices, Nano Lett. **8**, 3766 (2008).
[19] T. L. Cocker, V. Jelic, R. Hillenbrand, and F. A. Hegmann, Nanoscale terahertz scanning probe microscopy, Nat. Photon. **15**, 558 (2021).
[20] R. A. Kowalski, N. S. Mueller, G. Á lvarez-Pérez, M. Obst, K. Diaz-Granados, G. Carini, A. Senarath, S. Dixit, R. Niemann, R. B. Iyer *et al.*, Ultraconfined terahertz phonon polaritons in hafnium dichalcogenides, Nat. Mater. **24**, 1735 (2025).
[21] G. L. Carr, M. C. Martin, W. R. McKinney, K. Jordan, G. R. Neil, and G. P. Williams, High-power terahertz radiation from relativistic electrons, Nature (London) **420**, 153 (2002).
[22] S. Tammaro, O. Pirali, P. Roy, J.-F. Lampin, G. Ducournau, A. Cuisset, F. Hindle, and G. Mouret, High density terahertz frequency comb produced by coherent synchrotron radiation, Nat. Commun. **6**, 7733 (2015).
[23] G. Andonian, A. Cook, M. Dunning, E. Hemsing, G. Marcus, A. Murokh, S. Reiche, D. Schiller, J. B. Rosenzweig, M. Babzien *et al.*, Observation of coherent terahertz edge radiation from compressed electron beams, Phys. Rev. ST Accel. Beams **12**, 030701 (2009).
[24] S. Casalbuoni, B. Schmidt, P. Schmüser, V. Arsov, and S. Wesch, Ultrabroadband terahertz source and beamline based on coherent transition radiation, Phys. Rev. ST Accel. Beams **12**, 030705 (2009).
[25] A. Perucchi, S. Di Mitri, G. Penco, E. Allaria, and S. Lupi, The TeraFERMI terahertz source at the seeded FERMI free-electron-laser facility, Rev. Sci. Instrum. **84**, 022702 (2013).
[26] Z. Wu, A. S. Fisher, J. Goodfellow, M. Fuchs, D. Daranciang, M. Hogan, H. Loos, and A. Lindenberg, Intense terahertz pulses from SLAC electron beams using coherent transition radiation, Rev. Sci. Instrum. **84**, 022701 (2013).
[27] M. Veronese, R. Appio, P. Craievich, and G. Penco, Absolute bunch length measurement using coherent diffraction radiation, Phys. Rev. Lett. **110**, 074802 (2013).
[28] M. Helm, S. Winnerl, A. Pashkin, J. M. Klopf, J.-C. Deinert, S. Kovalev, P. Evtushenko, U. Lehnert, R. Xiang, A. Arnold *et al.*, The ELBE infrared and THz facility at Helmholtz-Zentrum Dresden-Rossendorf, Eur. Phys. J. Plus **138**, 158 (2023).
[29] M. Krasilnikov, Z. Aboulbanine, G. Adhikari, N. Aftab, A. Asoyan, P. Boonpornprasert, H. Davtyan, G. Georgiev, J. Good, A. Grebinyk *et al.*, First high peak and average power single-pass THz free-electron laser in operation, Phys. Rev. Accel. Beams **28**, 030701 (2025).
[30] A. Fisher, Y. Park, M. Lenz, A. Ody, R. Agustsson, T. Hodgetts, A. Murokh, and P. Musumeci, Single-pass high-efficiency terahertz free-electron laser, Nat. Photon. **16**, 441 (2022).
[31] A. Fisher, M. Lenz, A. Ody, Y. Yang, C. Pennington, J. Maxson, T. Hodgetts, R. Agustsson, A. Murokh, and P. Musumeci, Towards higher frequencies in a compact prebunched waveguide THz-FEL, Nat. Commun. **15**, 7582 (2024).
[32] R. Bonifacio, B. W. J. McNeil, and P. Pierini, Superradiance in the high-gain free-electron laser, Phys. Rev. A **40**, 4467 (1989).
[33] A. Gover, R. Ianconescu, A. Friedman, C. Emma, N. Sudar, P. Musumeci, and C. Pellegrini, Superradiant and stimulated-superradiant emission of bunched electron beams, Rev. Mod. Phys. **91**, 035003 (2019).
[34] Y. Liang, Z. Liu, Q. Tian, T. Li, X. Lin, L. Yan, Y. Du, R. Li, J. Shi, C. Cheng *et al.*, Widely tunable electron bunch trains for the generation of high-power narrowband 1-10 THz radiation, Nat. Photon. **17**, 259 (2023).
[35] Y. Liang, T. Li, J. Sun, Z. Liu, J. Yang, X. Wang, Y. Yu, Q. Tian, Z. He, H. Wang *et al.*, Superradiant terahertz free-electron laser driven by electron microbunch trains, Light Sci. Appl. **15**, 60 (2026).
[36] A. S. Weling and D. H. Auston, Novel sources and detectors for coherent tunable narrow-band terahertz radiation in free space, J. Opt. Soc. Am. B **13**, 2783 (1996).
[37] S. Bielawski, C. Evain, T. Hara, M. Hosaka, M. Katoh, S. Kimura, A. Mochihashi, M. Shimada, C. Szwaj, T. Takahashi *et al.*, Tunable narrowband terahertz emission from mastered laser–electron beam interaction, Nat. Phys. **4**, 390 (2008).
[38] Y. Shen, X. Yang, G. L. Carr, Y. Hidaka, J. B. Murphy, and X. Wang, Tunable few-cycle and multicycle coherent terahertz radiation from relativistic electrons, Phys. Rev. Lett. **107**, 204801 (2011).
[39] M. Dunning, C. Hast, E. Hemsing, K. Jobe, D. McCormick, J. Nelson, T. O. Raubenheimer, K. Soong, Z. Szalata, D. Walz *et al.*, Generating periodic terahertz structures in a relativistic electron beam through frequency down-conversion of optical lasers, Phys. Rev. Lett. **109**, 074801 (2012).
[40] S. Seletskiy, B. Podobedov, Y. Shen, and X. Yang, Seeding, controlling, and benefiting from the microbunching instability, Phys. Rev. Lett. **111**, 034803 (2013).
[41] E. Roussel, E. Ferrari, E. Allaria, G. Penco, S. Di Mitri, M. Veronese, M. Danailov, D. Gauthier, and L. Giannessi, Multicolor high-gain free-electron laser driven by seeded microbunching instability, Phys. Rev. Lett. **115**, 214801 (2015).
[42] Y. Kang, T. Li, Z. Wang, Y. Wang, C. Yu, W. Yin, Z. Gao, H. Xu, H. Luo, X. Wang *et al.*, Continuous terahertz band coverage through precise electron-beam tailoring in free-electron lasers, Nat. Photon. **20**, 96 (2026).
[43] X. Li, J. Sun, Y. Yu, J. Shao, J. Yang, Q. Zhou, H. Ding, L. Shi, K. Tao, C. Guo *et al.*, An injector testbed based on a direct current gun and an interchangeable very high frequency gun for superconducting continuous-wave free-electron lasers, J. Synchrotron Radiat. **32**, 838 (2025).
[44] P. Musumeci, C. Pellegrini, and J. B. Rosenzweig, Higher harmonic inverse free-electron laser interaction, Phys. Rev. E **72**, 016501 (2005).
[45] S. Y. Tochitsky, O. B. Williams, P. Musumeci, C. Sung, D. J. Haberberger, A. M. Cook, J. B. Rosenzweig, and C. Joshi, Efficient harmonic microbunching in a 7th-order

inverse-free-electron laser interaction, Phys. Rev. ST Accel. Beams **12**, 050703 (2009).

[46] D. Xiang, E. Hemsing, M. Dunning, C. Hast, T. O. Raubenheimer, S. Weathersby, and F. Fu, Demonstration of harmonic interaction in an undulator up to the 15th order, Phys. Rev. ST Accel. Beams **16**, 110701 (2013).

[47] K. Halbach, Physical and optical properties of rare earth cobalt magnets, Nucl. Instrum. Methods Phys. Res. **187**, 109 (1981).

[48] M. Borland, ELEGANT: A flexible SDDS-compliant code for accelerator simulation Report No. LS-287, Argonne National Lab., IL (US), 2000.

[49] S. Reiche, GENESIS 1.3: A fully 3D time-dependent FEL simulation code, Nucl. Instrum. Methods Phys. Res. A **429**, 243 (1999).

[50] E. Zeek, R. Bartels, M. M. Murnane, H. C. Kapteyn, S. Backus, and G. Vdovin, Adaptive pulse compression for transform-limited 15-fs high-energy pulse generation, Opt. Lett. **25**, 587 (2000).

[51] R. Bonifacio, C. Pellegrini, and L. M. Narducci, Collective instabilities and high-gain regime in a free electron laser, Opt. Commun. **50**, 373 (1984).

[52] E. A. Schneidmiller and M. V. Yurkov, Obtaining high degree of circular polarization at x-ray free electron lasers via a reverse undulator taper, Phys. Rev. ST Accel. Beams **16**, 110702 (2013).

[53] C. Emma, N. Sudar, P. Musumeci, A. Urbanowicz, and C. Pellegrini, High efficiency tapered free-electron lasers with a prebunched electron beam, Phys. Rev. Accel. Beams **20**, 110701 (2017).